The far-infrared emission line and continuum spectrum of the Seyfert galaxy NGC 1068[1]

Luigi Spinoglio

Istituto di Fisica dello Spazio Interplanetario, CNR, via Fosso del Cavaliere 100, I-00133 Roma, Italy

luigi@ifsi.rm.cnr.it

Matthew A. Malkan

Physics & Astronomy Dept., UCLA, Los Angeles, CA 90095, USA

malkan@astro.ucla.edu

Howard A. Smith

Harvard-Smithsonian CfA, 60 Garden St., Cambridge, MA 02138, USA

hsmith@cfa.harvard.edu

Eduardo González-Alfonso

Universidad de Alcalá de Henares, Departamento de Física, Campus Universitario, E-28871 Alcalá de Henares, Madrid, Spain

eduardo.gonzalez@uah.es

Jacqueline Fischer

Naval Research Laboratory, Code 7213, Washington DC 20375, USA

Jackie.Fischer@nrl.navy.mil

ABSTRACT

We report on the analysis of the first complete far-infrared spectrum (43-197μm) of the Seyfert 2 galaxy NGC 1068 as observed with the *Long Wavelength Spectrometer* (LWS) onboard the *Infrared Space Observatory* (ISO). In addition to the 7 expected ionic fine structure emission lines, the OH rotational lines at 79, 119 and 163μm were all detected in emission, which is unique among galaxies with full LWS spectra, where the 119μm line, where detected, is always in

absorption. The observed line intensities were modelled together with ISO *Short Wavelength Spectrometer* (SWS) and optical and ultraviolet line intensities from the literature, considering two independent emission components: the AGN component and the starburst component in the circumnuclear ring of $\sim$ 3kpc in size. Using the UV to mid-IR emission line spectrum to constrain the nuclear ionizing continuum, we have confirmed previous results: a canonical power-law ionizing spectrum is a poorer fit than one with a deep absorption trough, while the presence of a *big blue bump* is ruled out. Based on the instantaneous starburst age of 5 Myr constrained by the Br γ equivalent width in the starburst ring, and starburst synthesis models of the mid- and far-infrared fine-structure line emission, a low ionization parameter (U=$10^{-3.5}$) and low densities (n=100 cm^{-3}) are derived. Combining the AGN and starburst components, we succeed in modeling the overall UV to far-IR atomic spectrum of NGC 1068, reproducing the line fluxes to within a factor 2.0 on average with a standard deviation of 1.4. The OH 119 μm emission indicates that the line is collisionally excited, and arises in a warm and dense region. The OH emission has been modeled using spherically symmetric, non-local, non-LTE radiative transfer models. The models indicate that the bulk of the emission arises from the nuclear region, although some extended contribution from the starburst is not ruled out. The OH abundance in the nuclear region is expected to be $\sim 10^{-5}$, characteristic of X-ray dominated regions.

Subject headings: galaxies: individual (NGC 1068) – galaxies: active – galaxies: nuclei – galaxies: Seyfert – galaxies: emission lines – galaxies: starburst – infrared: galaxies.

1. INTRODUCTION

NGC 1068 is known as the archetypical Seyfert type 2 galaxy. It is nearby, luminous ($L_{IR} = 2 \times 10^{11} L_{\odot}$ Bland-Hawthorn et al. 1997), and it has been extensively observed and studied in detail from X-rays to radio wavelengths. With a measured redshift of z=0.0038 (Huchra et al. 1999) (corresponding to a distance of D=15.2 Mpc for H_0=75 km s^{-1} Mpc^{-1}), it provides a scale of only $\sim$ 74 pc/″. A central nuclear star cluster has an extent of $\sim$0.6″

[1]ISO is an ESA project with instruments funded by ESA Member States (especially the PI countries: France, Germany, the Netherlands and the United Kingdom) and with the participation of ISAS and NASA.

(Thatte et al. 1997) and a 2.3 kpc stellar bar observed in the near-IR (Scoville et al. 1988; Thronson et al. 1989) is surrounded by a circumnuclear starburst ring. Telesco et al. (1984) found that the infrared emission in NGC 1068 was due to both the Seyfert nucleus (which dominates the 10μm emission) and to the star forming regions in the bright $\sim$ 3kpc circumnuclear ring (which emits most of the luminosity at $\lambda > 30\mu m$). A $Br\gamma$ imaging study (Davies, Sugai & Ward 1998) showed a similar morphology and indicated that a short burst of star formation occurred throughout the circumnuclear ring of 15-16″ in radius within the last 4-40 Myr. CO interferometer observations revealed molecular gas very close to the nucleus ($\sim$0.2″) suggesting the presence of $\sim 10^8 M_\odot$ within the central 25pc (Schinnerer et al. 2000). Recent high resolution H_2 line emission mapping indicates the presence of two main nuclear emission knots with a velocity difference of 140 km/s, which, if interpreted as quasi-keplerian, would imply a central enclosed mass of $10^8 M_\odot$ (Alloin et al. 2001).

In this article, we present the first complete far-infrared spectrum from 43 to 197μm showing both atomic and molecular emission lines (§2). We model the far-IR continuum emission using a radiative transfer code and gray body functions (§3) and model the composite UV- to far-IR atomic emission line spectrum, from our data and the literature, using photoionization models of both the active nucleus (§4.1) and the starburst components (§4.2-4.3). Moreover, two different non-local, non-LTE radiative transfer codes have been used to model the OH lines (§5). Our conclusions are then given in §6.

2. OBSERVATIONS

NGC 1068 was observed with the Long Wavelength Spectrometer (LWS) (Clegg et al. 1996) on board the Infrared Space Observatory (ISO) (Kessler et al. 1996), as part of the Guaranteed Time Programme of the LWS instrument team. The full low resolution spectrum (43-197μm) of NGC 1068 was collected during orbit 605 (July 13, 1997). Two on-source full scans (15,730 seconds of total integration time) and two off-source (6' N) scans of the [CII]158μm line (3,390 seconds of total integration time) were obtained. On- and off-source scans had the same integration time per spectral step. Because of the design of the LWS spectrometer, simultaneously with the 158μm data, a short spectral scan of equal sensitivity to the on-source spectrum was obtained at sparsely spaced wavelengths across the LWS range.

The LWS beam is roughly independent of wavelength and equal to about 80 arcsec. The spectra were calibrated using Uranus, resulting in an absolute accuracy better than

30% (Swinyard et al. 1996). The data analysis has been done with ISAP[2], starting from the auto-analysis results processed through the LWS Version 7-8 pipeline (July 1998). To be confident that newer versions of the pipeline and calibration files did not yield different results, we have compared our data with the results obtained using pipeline 10.1 (November 2001) and we did not find significant differences in the line fluxes or the continuum.

All the full grating scans taken on the on-source position and the two sets of data on the off-source position were separately co-added. No signal was detected in the off-source coadds. The emission line fluxes were measured with ISAP, which fits polynomials to the local continuum and Gaussian profiles to the lines. In all cases the observed line widths were consistent with the instrumental resolution of the grating, which was typically 1500 km/sec. The integrated line fluxes measured independently from data taken in the two scan directions agreed very well, to within 10%. The on source LWS spectrum that resulted from stitching the ten LWS channels together using small multiplicative corrections in order to match the overlapping regions of each channel with its neighbors is shown in Fig. 1. LWS spectra of sources that are very extended within the instrument beam or that peak off center are typically affected by channel fringing in the continuum baseline (Swinyard et al. 1998). Fortunately, these spurious ripples are hardly noticeable in our LWS spectrum, presumably because the far-IR continuum is centrally concentrated towards the center of the LWS 80″ beam.

Besides the LWS observations, we also use the SWS observations presented by Lutz et al. (2000), to extend the wavelength and ionization-level coverage. Table 1 presents all the ISO line flux measurements including those from the SWS with their respective aperture sizes.

3. THERMAL CONTINUUM SPECTRUM

We have modeled the mid- and far-infrared spectral energy distribution (SED) of NGC 1068 by means of a non-local, spherically symmetric, radiative transfer code (González-Alfonso & Cernicharo 1997, 1999). We modeled the nuclear continuum emission closely following the approach by Cameron et al. (1993), and using the ISO-SWS fluxes reported by Lutz et al.

[2]The ISO Spectral Analysis Package (ISAP) is a joint development by the LWS and SWS Instrument Teams and Data Centers. Contributing institutes are Centre d'Etude Spatiale des Rayonnements (France), Institute d'Astrophysique Spatiale (France), Infrared Processing and Analysis Center (United States), Max-Planck-Insitut für Extraterrestrische Physisk (Germany), Rutherford Appleton Laboratories United Kingdom) and the Space Research Organization, Netherlands.

(2000). A central source with luminosity 1.5×10^{11} $L_\odot$ illuminates a spherically symmetric dust envelope with inner and outer radii of 1 and 200 pc, respectively. The envelope is divided into a set of spherical shells where the dust temperature is computed assuming that heating and cooling are equal. We assumed a standard silicate/amorphous carbon mixture with optical constants given by Draine (1985) and Preibisch et al. (1993). The density profile was assumed to be $\propto r^{-\beta}$, with β and the density at the inner radius regarded as free parameters. The predicted flux densities were compared with the continuum observed in the SWS spectrum by assuming that the bulk of the continuum in the 2-45 μm range arises from the nuclear region (see below). A reasonable fit to the observed mid-infrared SED is shown in Fig. 1, where $\beta = 1$ and, assuming a gas-to-dust mass ratio of 10^2, the averaged H_2 density at the inner radius is $< n_I(H_2) >= 1.7 \times 10^3$ cm^{-3}, the radial H_2 column density is $N(H_2) = 2.7 \times 10^{22}$ cm^{-2}, and the total mass is $M = 2.1 \times 10^7$ $M_\odot$. The values of $N(H_2)$ and M are in agreement with those inferred by Helfer & Blitz (1995).

The main weakness of our nuclear model is that the flux density at 30-50 μm is somewhat overestimated, a problem that could be more severe if there is a contribution to the continuum emission in the SWS aperture by the extended starburst at $\lambda > 30$ μm . On the other hand, the decomposition of the mid-infrared emission performed by Le Floc'h et al. (2001) with ISOCAM into the nuclear and extended contributions attributes to the nucleus, between 2 and 16 μm, significantly higher flux densities than those reported by Lutz et al. (2000) within the SWS aperture, suggesting that uncertainties in absolute calibration are affecting one or both data sets. Although our continuum model for the nuclear region is thus reasonable within the uncertainties, the nuclear continuum emission in the 30–50 μm range could be overestimated by a factor as high as 2. The latter is relevant for the analysis of the OH emission because, as we argue in section §5, the relative contributions of the nuclear and the extended components of the 30-50 μm continuum are important in discerning which component is responsible for the OH emission lines.

The complete far-infrared continuum emission is fitted in Fig. 1 by adding two components at 32 K and 20 K (Spinoglio, Andreani & Malkan 2002). These are gray body functions with a steep ($\beta = 2$) dust emissivity law. We identify the 32 K component with the starburst ring that is well delineated by the PAH 7.7 μm emission (Le Floc'h et al. 2001). Assuming a spherical shell with radius of 1.5 kpc and thickness of 0.3 kpc, the average H_2 molecular density of the 32 K component is ≈ 5 cm^{-3}. The total mass is 1.6×10^9 $M_\odot$ and 2×10^9 $M_\odot$ for the 32 K and 20 K components, respectively. These estimates are in good agreement with the $\sim 4 \times 10^9$ $M_\odot$ derived by Planesas et al. (1991) for the molecular ring.

4. THE FINE STRUCTURE LINES

To be able to better constrain the modeling of the line emission of NGC 1068, we have combined our far-infrared fine structure line measurements (Table 1) with ultraviolet, optical and infrared spectroscopic data from the literature (Kriss et al. 1992; Marconi et al. 1996; Thompson 1996; Lutz et al. 2000). The complete emission line spectrum of NGC 1068 from the ultraviolet to the far-IR includes several low-ionization lines that are primarily produced outside the narrow line region (NLR) of the active nucleus, as well as intermediate ionization lines that originate from both starburst and AGN emission. For this reason, we find that no single model satisfactorily explains all the observed emission lines. We identify two main components:

- an AGN component (the NLR), exciting the high ionization lines and contributing little to the low-to-intermediate ionization lines;
- a starburst component in the circumnuclear ring of the galaxy (e.g. Davies, Sugai & Ward 1998) that produces the low ionization and neutral forbidden lines and some of the emission in the intermediate ionization lines. This component should also produce emission associated with photo-dissociation regions (PDRs) (e.g. Kaufman et al. 1999), at the interface with the interstellar medium of the galaxy.

In this section, we will examine separately the two components that produce the total fine structure emission line spectrum of NGC 1068, namely the AGN and the starburst, for which we propose two different computations, and we add together these components to reproduce the overall observed spectrum from the UV to the far-IR in §4.3.

4.1. Modeling the AGN

The first photoionzation model predictions of the mid to far-infrared emission line spectra of the Narrow Line Regions (NLR) of active galaxies were presented by Spinoglio & Malkan (1992), well before the ISO observations could be collected. Alexander et al. (2000) used the observed high ionization emission lines to model the obscured ionizing AGN continuum of NGC 1068 and found that the best-fit spectral energy distribution (SED) has a deep trough at 4 Rydbergs, which is consistent with an intrinsic "big blue bump" that is partially obscured by $\sim 6 \times 10^{19}$ cm^{-2} of neutral hydrogen interior to the NLR. Following their results, we have simulated their models, although using a different photoionization code, *CLOUDY* (Version 94.00 Ferland 2000), and then we have varied the shape of the ionizing continuum

to include the ionizing continuum derived in Pier et al. (1994). Our goal was to test if the Alexander et al. (2000) results were unique and to fit the remaining emission by a starburst component, and thereby to derive a composite model of the complete emission line spectrum of NGC 1068.

Specifically, we explore three plausible AGN SEDs. Model A assumes the best fit ionizing spectrum derived by Alexander et al. (2000), i.e. with a deep trough at 4 Rydberg (log$f$ = -27.4, -29.0, -27.4, -28.2 at 2, 4, 8 and 16 Ryd, respectively). An intrinsic nuclear spectrum of NGC 1068 has also been inferred by Pier et al. (1994). Model B assumes the original ionizing spectrum derived from Pier et al. (1994). Model C assumes an SED with a *Big Blue Bump* superposed on the Pier et al. (1994) ionizing continuum (log$f$ = -25.8, -25.8, -25.8, -27.4 at 2, 4, 8 and 16 Ryd, respectively) as expected for the thermal emission of an accretion disk around a central black hole. These three AGN ionizing continua are plotted in Fig. 2. For each of models A, B, and C, we have used two component models with the same parameters as in Alexander et al. (2000): component 1 has a constant hydrogen density of $10^4 cm^{-3}$, an ionization parameter U=0.1, a covering factor c=0.45, a filling factor of 6.5×10^{-3} with a radial dependence of the form r^{-2}, and extends from $\sim$ 21 to $\sim$ 109 pc from the center; component 2 has a density of 2×10^3 cm^{-3}, an ionization parameter U=0.01, a covering factor of c=0.29, a filling factor of 6.5×10^{-4} without any radial dependence, and extends from $\sim$ 153 to $\sim$ 362 pc from the center. We have also assumed the "low oxygen" abundances adopted by Alexander et al. (2000), in order to be able to compare our results with theirs. The inner and outer radii of the emission regions of the two components, 21, 109, 153 and 362 pc, correspond to angular distances of about 0.26, 1.4, 1.9 and 4.5 $''$, respectively. Table 2 reports the predicted line fluxes of the three AGN models, A, B, and C, together with the observed line fluxes: the line fluxes are given for each of the two components 1 and 2, which are treated as independent, and the total flux for each model is simply the sum of the fluxes of the two components.

We can see from Table 2 that only the AGN A and B models, and not the AGN C model, reproduce most of the observed high ionization line fluxes. The low and intermediate ionization lines, are expected to have partial or full contributions from starburst and PDR components (see §4.2). This first result rules out the presence of a "big blue bump" in the ionizing continuum of NGC 1068. To be able to compare the modeled ultraviolet and optical lines with the observations, we also listed in Table 2 and 3 their dereddened fluxes, assuming two values for the extinction: E_{B-V} = 0.4 mag (Malkan & Oke 1983) and E_{B-V} = 0.2 mag (Marconi et al. 1996). We find that the AGN B model overpredicts several of the intermediate ionization lines, such as [SIV]10.5μm, [NeIII]15.6μm and [SIII]18.7μm, and this discrepancy increases when adding the starburst component because these lines are also copiously produced by that component (see next section). On the other hand, the

[NeII]12.8μm emission is underpredicted so much so that even with the inclusion of the starburst component it cannot be reproduced with this model. As we discuss further in §4.3, a composite AGN/starburst model using AGN model A is able reproduce the [NeII]12.8μm emission to within the measurement errors.

4.2. Modeling the starburst ring

NGC 1068 is known to emit strong starburst emission from the ring-like structure at a radial distance of 15 – 16″ from the nucleus (total size of $\sim$ 3kpc), traced for example by the Br γ emission (Davies, Sugai & Ward 1998). Mid-IR line imaging observations of NGC 1068 have been published by Le Floc'h et al. (2001) based on ISOCAM CVF observations. They presented an image of the 7.7 μm PAH feature that shows constant surface brightness above the 4th coutour near the nucleus. This suggests that star formation is occuring in the direction of the nucleus so that nuclear spectra will include some emission from star formation. In the case of the SWS observations that we are modeling (reported by Lutz et al. (2000)), three apertures were used at different wavelengths with the two largest also including portions of the brighter starburst ring (see Table 1). To estimate how much of the starburst emission is contained in the different apertures used in the observations, we have used a continuum subtracted image in the 6.2 μm feature produced by C. Dudley (private communication) using the same ISOCAM CVF data set examined by Le Floc'h et al. (2001). The 6.2 μm feature is more isolated than the 7.7 μm feature, which is blended with the 8.7 μm feature and the silicate absorption feature, but the image compares well with the published 7.7 μm image though we have zeroed out the residuals in a 3×12 arcsec^2 region centered on the nucleus. Based on this image, the SWS 14×20, 14×27 and 20×33 arcsec^2 slits contain 13, 23 and 46% of the 6.2 μm flux contained in the LWS beam respectively, without correction for the neglected region of poor residuals (oriented at 45° to our synthetic SWS slits). Since PAH features are thought to be a good tracer of PDRs and their associated startbursts, we adopt these percentages in our model predictions of SWS line strengths in the starburst models presented in this section. Further, in fitting our starburst models to the observations, we have abandoned the requirement to obtain the absolute fluxes observed at earth, but rather normalized the emission to the intensity of the [NII]122μm line observed with the LWS, because it has virtually no emission from any AGN model.

We have chosen the starburst synthesis modeling program Starburst99 (Leitherer et al. 1999), to produce input ionizing spectra for the *CLOUDY* photoionization code. We compared the predictions of two different ionizing continua shown in Fig. 3. The first is based on an instantaneous star formation law, with a total mass of M = 10^6 M$_\odot$, while the

second is based on a continuous star formation law with a star formation rate of 1 $M_\odot$ yr^{-1}. For both types of models we adopted an age of 5 Myr, a Salpeter IMF (α=2.35), a lower cut-off mass of 1 $M_\odot$, an upper cut-off mass of 100 $M_\odot$, solar abundances (Z=0.020) and nebular emission included. These particular ionizing continua were selected because they are consistent with the Br γ equivalent width observed by Davies, Sugai & Ward (1998) in the starburst ring. We have estimated that the Br γ equivalent width in each of the individual regions of the map of Davies, Sugai & Ward (1998) is in the range 110-180 Å. According to the Leitherer et al. (1999) models (see their figures 89 and 90), for a value of log(W(Br γ, Å)) $\geq$ 2 only instantaneous models with ages less than $\sim 6\times 10^6$ yrs are allowed; similarly, only continuous models with ages less than $\sim 10^7$ yrs are permitted.

We report in Table 3 the line fluxes predicted for six different starburst models, chosing the above instantaneous star formation law model as the input ionizing continuum and using *CLOUDY* with densities of n_H = 10, 100, 1000 cm^{-3} and ionization parameters of Log U = -2.5, -3.5. We have also run models with the continuous star formation law presented above, but we do not list their results in Table 3, because the differences in the line flux predictions are insignificant, while line fluxes strongly depend on the choice of density and ionization parameter, as can be seen from Table 3. This result is not surprising because the two ionizing continua as derived from the starburst models are in fact quite similar in their shape and we are not computing absolute line intensities, but only their ratios to a particular observed line. We have also tried continuous starburst models with much longer ages (10, 20 and 100 $\times$ 10^6 years) but, because the shape of the ionizing continuum again does not change significantly, the resulting emission line spectrum was indistinguishable from that one derived from the models with an age of 5 $\times$ 10^6 years.

In all models the abundances were those of HII regions with grains included. The integration was allowed to run until the temperature of the gas in the cloud cooled to T=50 K in order to include the photodissociation regions present at the interfaces of HII regions and molecular clouds.

It is clear from Table 3 that the models with the higher ionization parameter (log U = -2.5) can easily be ruled out, because their emission in many intermediate ionization lines is far too high (see e.g. [OIV]26μm, [OIII]51,88μm, [NIII]57μm). Moreover, the intermediate density of n_H = 100 cm^{-3} gives the best fit to the observed lines, taking into account that the AGN component must be added to reproduce the total flux as shown §4.3.

We estimate the average PDR parameters using the models of Kaufman et al. (1999) and the contour plots in Luhman et al. (2003), the measured [C II]158 and [O I]145 μm line fluxes (but not the [O I]63 μm line flux which may be affected by absorption and/or shocks), and the FIR flux integrated over the LWS spectrum, which we find to be 1.3 $\times$ 10^{-8} ergs

cm^{-2} sec^{-1}. Here we assume that the [C II] line emerges predominantly from PDRs due to the strong starburst, rather than the diffuse ionized medium. With this assumption, the average PDR gas density and UV radiation field are $n_{H_2} \sim 1000$ and $G_0 \sim 300$ respectively. We note that if instead we assume that the [C II] line flux is dominated by the diffuse ionized medium, using the correction factor estimated by Malhotra et al. (2001), we obtain a similar gas density $n_{H_2} \sim 1500$ but a significantly higher interstellar radiation field $G_0 \sim 1500$. For both cases, the parameters derived are in the range of those of the normal galaxies in the Malhotra et al. (2001) sample, consistent with the assumption that most of the FIR flux originates in the starburst ring.

4.3. Adding the two components

Summing the line intensities of each one of the two components, the composite spectrum of NGC 1068 can be derived and compared with the observed one. We have chosen three combinations to compute the composite models, each one with a different AGN model, while we adopted the starbust model with $n_H = 100$ cm^{-3} and Log U = -3.5: 1) the first one (that we name CM1, for Composite Model 1) with the AGN ionizing continuum as suggested by Alexander et al. (2000) (model AGN A); 2) the second (CM2) with the original Pier et al. (1994) (model AGN B); 3) the third (CM3) with the hypothetical bump (model AGN C). The results of these three composite models are given in Table 4, compared to the observed and dereddened values, assuming the two choices for the extinction (see §4.1). We also show the results of the three composite models in a graphical way in Fig. 4, where the modeled to the observed flux ratio is given for each line for the case of an extinction of E_{B-V}=0.2 mag.

A simple χ squared test of the three models resulted in a reduced χ square of 11.9, 24.6 and 241 for the three models CM1, CM2 and CM3, respectively. We note that for CM1 the line fluxes are reproduced to within a factor of 2.0 on average with a standard deviation of 1.4 including all of the detected lines for the model with E_{B-V}=0.2 mag. The infrared lines only are reproduced to within a factor of 1.6 on average with a standard deviation of 0.9.

5. THE OH LINES

5.1. General remarks

In NGC 1068, we detect three of the OH rotational lines, all in emission. As shown in the energy level diagram of Fig. 5, two of them are fundamental lines, connecting the ground state $^2\Pi_{3/2}3/2$ level with the $^2\Pi_{3/2}5/2$ (the in-ladder 119 μm line) and with the $^2\Pi_{1/2}1/2$

level (the cross ladder 79 μm line). The third line is the lowest transition of the $^2\Pi_{1/2}$ ladder: the 163μm line between the J=3/2 and J=1/2 levels. The detected line fluxes are given in Table 1. The fact that these three lines are *all* in emission is in striking contrast with the OH lines observed in other bright infrared galaxies, such as Arp 220 (Fischer et al. 1999; González-Alfonso et al. 2004), Mrk 231 (Harvey et al. 1999), NGC 253 (Bradford et al. 1999), and M 82 (Colbert et al. 1999), in which the 119 μm fundamental is in absorption. The 79μm line is sometimes seen in emission and sometimes in absorption; the 163μm line is always seen in emission. In addition to the detections, the ISO-LWS and SWS observations provide upper limits on fluxes of the other four lines that arise between the lowest six rotational levels. The LWS spectra in the vicinity of the detected lines (and of one of the upper limits), are shown in detail in Fig. 6 (histograms). In this section we discuss the physical conditions necessary to excite these lines, their probable location within NGC 1068, and detailed model fits to their fluxes. A comparison between the observed and modeled line fluxes is given in Table 5 and shown in Fig. 6.

5.2. The excitation mechanism of the OH lines

The unique OH emission line spectrum of NGC 1068 can provide a powerful way to help discriminate between the properties of the molecular clouds in NGC 1068 and the clouds in other galaxies in which OH has been observed. Before describing our detailed radiative transfer calculations, it is instructive to discuss some conclusions that are model-independent. The emission in the OH $\Pi_{3/2}\,5/2 - 3/2$ line at 119 μm cannot be explained by absorption of far-infrared photons followed by cascade down to the upper $\Pi_{3/2}\,5/2$ level of the transition. Rather, we argue that collisional excitation dominates. Figure 5 shows the energy level diagram of OH. There are only two possible paths to excite the 119 μm line via absorption of far-infrared photons: via the 35 μm and/or the 53 μm ground-state lines. Excitation by either of these routes has other observable consequences. In the case of simple radiative cascading, the Einstein-A coefficients of the lines involved in the corresponding cascades are such that if the 35 μm absorption path were responsible for the observed 119μm line flux, then the OH $\Pi_{1/2}\,5/2 - 3/2$ line at 98.7 μm would be approximately 5 times stronger than the 119 μm line, while the 98.7 μm line is not detected. Hence this possibility is ruled out. Similarly, if absorption in the 53μm line were responsible for the observed 119μm line flux, then the 163μm line would be about 5 times stronger than the 119 μm line, which it is not. We can therefore conclude from the constraints provided by the other far-infrared OH lines that the 119μm emission line is not the result of radiative absorption and cascading. The implication is that OH excitation through collisions is more important in NGC 1068 than in the other observed galaxies and therefore that the gas responsible for the observed

emission in the 119μm line resides predominantly in relatively dense and warm enviroments in comparison with these other sources.

The other two observed emission lines, unlike the 119 μm line, need not be collisionally dominated. In the case of the $\Pi_{1/2}$ 3/2−1/2 163μm line, the most likely excitation mechanism is absorption of photons emitted by dust in the 53 and 35 μm lines followed by radiative cascade. The upper level of this transition is 270 K above the ground state (Fig. 5), so that excitation through collisions is expected to be ineffective in this line. The excitation mechanism of the $\Pi_{1/2} - \Pi_{3/2}$ 1/2 − 3/2 79 μm line could be a mixure of collisional and radiative pumping. The upper level of this transition is 182 K above the ground state, so that a warm and dense region could, at least partially, excite the line through collisions. Nevertheless, the line could be also excited through the same infrared pumping mechanism that results in the observed 163 μm line emission.

In conclusion, the 119 μm line is collisionally excited, whereas absorption of photons emitted by dust in the 53 and 35 μm lines probably dominates the excitation of the 163 μm line. The 79 μm OH line may in principle be excited through both mechanisms.

5.3. Constraints on the spatial origin of the 119 μm OH line

In NGC 1068 two regions with very different physical conditions can account for the observed OH emission as discussed above: the compact nuclear region, and the ring and bar where the starburst is taking place. A warm and dense region is required to account for the observed 119 μm line emission, given that the line is collisionally excited, so the warm and dense nuclear region around the AGN should be considered a good candidate, despite its small size ($\sim 5''$; e.g. Planesas et al. 1991; Schinnerer et al. 2000), for the following reasons:

(*i*) It is warm: there are $\sim 10^3$ $M_\odot$ of hot H_2 ($\sim$ 2000 K) distributed over $\sim 5''$ (Blietz et al. 1994). From the CO (4-3) to (1-0) line intensity ratio, Tacconi et al. (1994) derive $\sim$ 80 K for the bulk of the molecular gas, with a mass of $\sim 3 \times 10^7$ $M_\odot$ enclosed in within the central 4″ (Helfer & Blitz 1995). Lutz et al. (2000) have reported the detection of pure H_2 rotational lines within the ISO-SWS aperture, and estimated $\sim 2.5 \times 10^7$ $M_\odot$ at $\sim$ 200 K, but these lines may also arise, at least partially, from the inner regions of the 3 kpc starburst ring.

(*ii*) The molecular clouds within the nuclear region are dense, although there is some dispersion in the values derived by several authors based on HCN emission: Tacconi et al. (1994) derived an H_2 density of $\sim 10^5$ cm^{-3}, whereas subsequent observations and

analysis by Helfer & Blitz (1995) yielded a density of $\sim 4 \times 10^6$ cm^{-3}. An intermediate density of $\sim 5 \times 10^5$ cm^{-3} from HCN and CS, and lower for other tracers, has been recently derived by Usero et al. (2004).

(*iii*) The OH abundance is expected to reach high values in regions exposed to strong incident UV fields (PDRs, Sternberg & Dalgarno 1995), and in particular in X-ray dominated regions (XDRs, Lepp & Dalgarno 1996). The remarkable chemistry found by Usero et al. (2004) in the circumnuclear disk of NGC 1068 is indicative of an overall XDR and suggests a high OH abundance in the nuclear region.

Given that the OH 119μm line is collisionally excited, the possibility that the line might arise from the nuclear region can be checked by computing the amount of warm gas required to account for the observed emission:

$$M_w(\mathrm{M}_\odot) = 1.6 \times 10^7 \times \left[\frac{10^{-5}}{X(\mathrm{OH})}\right] \times \left[\frac{5 \times 10^5\,\mathrm{cm}^{-3}}{n(\mathrm{H}_2)}\right] \times \left[\frac{4.3 \times 10^{-11}\,\mathrm{cm}^3\,\mathrm{s}^{-1}}{< c_{lu} >}\right], \quad (1)$$

where $X(\mathrm{OH})$ is the OH abundance relative to H_2, and $< c_{lu} >$ is the collisional rate for excitation from the ground $\Pi_{3/2}\,3/2$ level to the $\Pi_{3/2}\,5/2$ one. Equation 1 assumes that, although the line could be optically thick, it is effectively optically thin, and makes use of the observed flux of 1.2×10^{-12} erg s^{-1} cm^{-2}. The reference value for the collisional rate, $< c_{lu} >= 4.3 \times 10^{-11}$ cm^3 s^{-1}, corresponds to gas at 80 K (Offer et al. 1994); it decreases by a factor of ≈ 2.7 for gas at 50 K and increases by a factor of 3 for gas at 200 K.

The reference OH abundance we use in this estimate, 10^{-5}, is the result of two separate studies: first, calculations of molecular abundances by Lepp & Dalgarno (1996) have shown that the OH abundance in XDRs is expected to be about two orders of magnitude higher than the abundance of HCN and HCO^+. The authors in fact suggested the possibility that the high HCN/CO ratio observed in the nuclear region of NGC 1068 could be a consequence of enhanced X-ray ionization. Second, the possibility of a chemistry dominated by X-rays has found support from observations by Usero et al. (2004), who derive abundance ratios of HCN, HCO^+, and CN in general agreement with predictions for XDRs. Since the HCN abundance derived by Usero et al. (2004) is $\sim 10^{-7}$, $X(\mathrm{OH})$ in XDRs could attain values as high as 10^{-5}. On the other hand, the density of 5×10^5 cm^{-3} derived by Usero et al. (2004) has been adopted as the reference value in eq. 1. Finally, from the continuum models discussed in §3, the mass of gas we derive for the nuclear region is $\sim 2 \times 10^7$ M$_\odot$, similar to the value required in eq. 1. From these estimates we conclude that, if the OH abundance is as high as $\sim 10^{-5}$ (i.e. if the predictions for XDRs are applicable to the nuclear region of NGC 1068), the bulk of the OH 119 μm line could arise there. This possibility would naturally explain why NGC 1068 is unique in its 119 μm line emission among galaxies with full LWS spectra.

Finally we ask whether the OH 119μm line could arise from an even more compact region, i.e., from a torus with a spatial scale of 1 pc surrounding the central AGN. According to typical parameters given by Krolik & Lepp (1989), a torus is expected to be hot ($\sim 10^3$ K), could have densities of 10^7 cm^{-3}, and therefore a mass of $\sim 10^5$ M$_\odot$. Also, the OH abundance is expected to be very high, $5 \times 10^{-5} - 10^{-4}$. Eq. 1 shows that the relatively low mass of the torus (about 2 orders of magnitude lower than the entire nucleus) could be compensated by the the higher density, OH abundance, and temperature expected there, so that this possibility cannot be neglected.

The reference values for the nuclear abundance and density adopted in eq. 1 are rather uncertain (and possibly extreme). The continuum models of §3 indicate that the mass associated with the 32 K dust component, which is identified with the starburst ring, is 1.6×10^9 M$_\odot$. If $\sim 5\%$ of this mass corresponds to warm molecular gas rich in OH, the amount of extended warm gas is $\sim 8 \times 10^7$ M$_\odot$. According to eq. 1, the OH emission at 119 μm can then also be explained as arising in the ring if the associated PDRs, with assumed OH abundance of 2×10^{-6} (Sternberg & Dalgarno 1995; Goicoechea & Cernicharo 2002; González-Alfonso et al. 2004), have densities of a few $\times 10^5$ cm^{-3}. Since Papadopoulos & Seaquist (1999b) found that most of the extended molecular gas resides in dense, compact clouds, this scenario seems also possible. However, the continuum from the starburst at 119 μm is strong, so that one expects that eq. 1 is in this case underestimating M_w, and the quoted physical parameters, X(OH) and n(H$_2$), are lower limits. The effect of dust emission is discussed in detail below.

In conclusion, a definitive answer to the issue of the spatial origin of the OH 119 μm emission cannot be inferred from only the flux observed in the 119 μm line. Nevertheless, useful constraints on this subject are given: the line could be either explained as arising from the nucleus, with a required OH abundance $\sim 10^{-5}$, or from the extended ring, with OH abundance $> 2 \times 10^{-6}$ and density $>$ a few $\times 10^5$ cm^{-3}. Nevertheless, the radiative transfer models described below, which take into account the effect of the continuum emission and the excitation of the 79 and 163 μm lines, point towards a nuclear origin of the OH emission.

5.4. Outline of the models

Analysis of the OH 79 and 163 μm lines requires the use of detailed radiative transfer calculations since, as pointed out above, the emission in these lines is expected to be strongly influenced by absorption of far-infrared continuum photons. We therefore proceeded to model the OH lines with two different codes, and confirmed that the results were in good agreement with each other. One of them, described in González-Alfonso & Cernicharo (1997, 1999),

has been recently used to model the far-infrared spectrum of Arp 220 (González-Alfonso et al. 2004), and the other is a Monte Carlo radiative transfer code used as part of a detailed study of all the OH lines observed by ISO in galaxies (Smith 2004; Smith et al. 2004). The latter was developed by the Submillimeter Wave Astronomy Satellite (SWAS) mission (Ashby et al. 2000), and is a modification of the original Bernes code. Both methods are non-local, non-LTE, assume spherical symmetry, and include a treatment of continuum photons from dust mixed in with the gas. Also, both codes take input as a series of concentric shells, each of which is assigned a size, gas and dust temperature, H_2 density, velocity and turbulent velocity width, and molecular abundance relative to H_2. The statistical equilibrium populations of OH in each spherical shell are computed by including the excitation by dust emission, excitation through collisions, and effects of line trapping. We ran two models to simulate the nucleus of the galaxy and the starburst extended ring, described in §5.4.1 and 5.4.2.

5.4.1. Models for the nuclear emission: constraints on the spatial origin of the 79 and 163 μm OH lines

We present models for the nuclear OH emission that *implicitly assume that the 119 μm emission line arises from the nuclear region*: $X(\mathrm{OH}) = 10^{-5}$ is adopted, as well as densities $\sim 5 \times 10^5$ cm^{-3} for the bulk of the emitting gas. By assuming a pure nuclear origin for the 119 μm line, we check whether the other two OH lines could, in such a case, arise from the same nuclear region or require a more extended spatial origin.

The models use dust parameters derived from the nuclear dust model described in §3. The gas temperature is assumed to be equal to the dust temperature (Fig. 1b). In order to avoid overestimation of the continuum flux at the important wavelengths of 35 and 53 μm (see section 3), we have decreased the dust abundance by a factor of 2, so that the predicted flux in the 35–53 μm range is 40-50 Jy.

The H_2 densities derived from the dust model (i.e. a peak density of $< n_I(\mathrm{H_2}) >= 1.7 \times 10^3$ cm^{-3} at the inner radius) are not compatible with the densities inferred from different molecular tracers. This indicates that the medium is extremely clumped, as has been also argued elsewhere (e.g. Cameron et al. 1993; Tacconi et al. 1994). In order to account approximately for this clumpiness in our models, the following strategy is adopted: we use the "real" $n(\mathrm{H_2}) \sim 5 \times 10^5$ cm^{-3} values for the bulk of the gas, and compute the volume filling factor $f_v =< n(\mathrm{H_2}) > /n(\mathrm{H_2})$, where the average value is that inferred from the dust model. The expected abundances of OH and the dust relative to H_2, $X(\mathrm{OH})$ and $X(\mathrm{dust})$, are then multiplied by f_v, so that the right OH and dust column densities are used

in the calculations together with the right density values. The same density profile r^{-1} that was used in the dust model is adopted, so that f_v is uniform throughout the nuclear region.

The modeled fluxes are convolved with the ISO-LWS grating resolution and are compared with the data in Fig. 6. Solid black lines show the results for the nuclear model that assumes $X(\mathrm{OH})=10^{-5}$ and $f_v = 2.3 \times 10^{-5}$, the later value implying a density in the outer regions (where the bulk of the emission is generated) of 5×10^5 cm^{-3}. The OH column density is $N(\mathrm{OH}) = 2.7 \times 10^{17}$ cm^{-2}. Besides the 119 μm line, the model reproduces the emission in the 79 and 163 μm lines and is consistent with the upper limits given in Table 5.

We also checked the excitation mechanism of the other OH lines by generating an additional model with the same parameters as above except for the continuum emission, which is now turned off. In this model, therefore, the lines are excited exclusively through collisions with H_2. The resulting flux of the 119 μm line remains unchanged when the dust emission is ignored, confirming that the line is collisionally excited. On the other hand, the flux densities of the 79 and 163 μm lines decrease in the "pure-collisional" model by factors of 2 and 5, respectively, showing that the emission in these lines is much more affected by radiative pumping. We conclude that, if the OH abundance in the nucleus were high enough to account for the collisionally excited 119 μm line, the observed fluxes in the 79 and 163 μm lines can also be explained as arising in the same nuclear region.

5.4.2. Models for the starburst emission

Two simple different approaches have been used to model the OH emission from the starburst. First, we have roughly modeled the whole starburst region as a spherical shell with external radius of 1.5 kpc, thickness of 0.3 kpc, and average H_2 density $< n_I(\mathrm{H_2}) >=$ 4.8 cm^{-3}, so that the corresponding continuum emission is reproduced with $T_d = 32$ K (section 3). As shown in section 5.3, the OH 119 μm emission requires densities of a few $\times 10^5$ cm^{-3}, so that we have assumed a volume filling factor $f_v = 10^{-5}$ and therefore a "real" density $n(\mathrm{H_2}) = 4.8 \times 10^5$ cm^{-3}. The kinetic temperature is assumed to be $T_k = 100$ K, and the OH abundance is $X(\mathrm{OH}) = 2 \times 10^{-6} \times f_h$, where $f_h = 0.05$ is the assumed fraction of warm gas. The result of this model is shown in Fig. 6 (upper dotted lines). The 119 μm line is reproduced, but the flux densities of both the 79 μm and 163 μm lines are strongly underestimated. The reason is that the model implicitly assumes that the continuum emission, responsible for the excitation of those lines, arises from a very large volume, so that the *radiation density* is weak and has negligible effect on the line excitation.

Since the OH emission should arise from compact, discrete PDRs in the vicinity of O or

early B stars, where the continuum infrared radiation density is expected to be stronger than assumed above, we have also tried an alternative approach, which consists of modelling an individual "typical" cloud of the starburst. We first model the continuum from an individual cloud by assuming a central heating source and computing the dust equilibrium temperatures at each radial position that result from the balance of heating and cooling. The continuum model is adopted if (*i*) leaving aside a scaling factor (N_c, the number of clouds in the ensemble), the resulting SED is similar to that of the far-infrared emission of the starburst (i.e. the 32 K component found in section 3); the value of N_c is determined by requiring that the absolute continuum flux from the ensemble of clouds is equal to that observed for the 32 K component; and (*ii*) we require that the total mass of the ensemble does not exceed the mass inferred from the non-nuclear region ($< 4 \times 10^9$ $M_\odot$). Once the continuum is fitted, calculations for OH are performed by assuming $T_k = T_d$, and $X(\mathrm{OH}) = 2 \times 10^{-6}$.

Several models with various density profiles were found to match the above two requirements. The common characteristic of all of them is the relatively high column density of the individual clouds, $N(\mathrm{H_2}) > 10^{23}$ cm^{-2}, which is a consequence of the low effective dust temperature (32 K) of the SED. The results of the simplest model, characterized by a flat density profile, $n(\mathrm{H_2}) = 5 \times 10^5$ cm^{-3}, are given here for reference. With a radius of 5×10^{17} cm, a stellar luminosity of 2×10^4 $L_\odot$, and $N_c = 4 \times 10^6$, the resulting SED is similar to that of the 32 K component (§3). For these clouds we obtain a total mass of 1.8×10^9 $M_\odot$. The predicted OH emission/absorption is shown in Fig. 6 (lower dashed lines). In spite of the relatively high density and temperatures (28-250 K) throughout the cloud, the 119 μm line is predicted to be too weak, and the 79 μm line is predicted in absorption. We have found this result quite general: in models where the OH abundance is high enough and the radiation density becomes strong enough to pump the 163 μm emission, the continuum at 79 and 119 μm is absorbed by OH and the predicted emission in the corresponding lines is reduced. Models that assume a density profile of r^{-1} generally predict the 119 μm line in absorption. In some models where the OH abundance was allowed to vary with radial position, the 79 μm line was predicted in emission but by far too weak to account for the observed flux density.

In conclusion, no starburst model is found to reproduce satisfactorily the emission observed in the three OH lines. If the local infrared radiation density is strong enough to pump the 163 μm line, the other two OH lines are expected to be weak or in absorption. Furthermore, the high density assumed for the starburst region would produce a relatively high HCN/CO intensity ratio, which is on the contrary ~ 0.01 in the spiral arms (Helfer & Blitz 1995). Finally, the PDR models described in $4.2 indicate a density of 1\text{-}1.5 \times 10^3$ cm^{-3}, i.e. a density much lower than that required to account for the flux density of the OH 119 μm line. Therefore, and despite the simplicity of our models, taken together the analysis of

the OH lines and the derived PDR parameters indicate that the bulk of the OH emission arises from X-ray dominated nuclear regions.

6. CONCLUSIONS

The main results of this article can be summarized as follows:

- The complete far-infrared (50-200μm) spectrum of NGC 1068 has been observed for the first time. The 50-200μm continuum can be interpreted as thermal dust emission due to a nuclear component with a luminosity of 1.5×10^{11} $L_{\odot}$ illuminating a spherically symmetric dust envelope with inner and outer radii of 1 and 200 pc, respectively, and two additional components at temperatures of 20 and 32K, assuming a steep (β=2) dust emissivity law.

- The far-infrared ISO-LWS spectrum has been complemented with the mid-infrared data of ISO-SWS and with shorter wavelength (UV, optical and near-IR) data from the literature to assemble a composite atomic spectrum as complete as possible with the aim of modeling the different line emission components at work. This approach has been necessary especially because of the poor spatial resolution of the ISO spectrometers, which were not able to spatially separate the emission components. The lines have been interpreted as arising from two physically distinct components: the AGN component and a starburst component, the first one nuclear and the second one located in the ring at a radius of 15-16 $''$ from the nucleus. The density and ionization parameter of the $\sim 5 \times 10^6$ year old starburst are found to be $n_H \sim 100$ cm^{-3} and log U = -3.5, respectively. Three composite models have been computed with different AGN components: the first one has the ionizing continuum as derived from Alexander et al. (2000), showing a deep trough at energies of a few Rydberg; the second has the monotonically decreasing ionizing continuum given by Pier et al. (1994) and the third has a "big blue bump". Two values of the visual extinction (E_{B-V} = 0.2 and 0.4) have been adopted to correct the optical and ultraviolet line fluxes for the reddening. The agreement between the composite model with an AGN ionizing continuum characterized by the deep trough suggested by Alexander et al. (2000) is very satisfactory, taking into account both the simplicity of the photoionization models chosen to avoid dealing with too many free parameters and the large number of lines which originate in different physical regimes. The agreement between the observed spectrum and what is predicted using the canonical ionizing continuum is poorer, while the presence of a big blue bump is ruled out.

- The unique OH emission in the 119 μm line cannot be explained in terms of OH excitation through absorption of 35 and 53 μm photons emitted by dust, but rather it is collisionally excited. This indicates the presence of a warm and dense region with high OH abundance. A simple excitation analysis yields two main alternatives for the *spatial origin* of the observed 119 μm line emission: (*i*) the nuclear region, with 2×10^7 $M_\odot$ of warm gas (80 K), an average density of $n(H_2) = 5 \times 10^5$ cm^{-3}, and an OH abundance of $\sim 10^{-5}$; (*ii*) the starburst region, if $\sim 5\%$ of the associated mass ($\sim 8 \times 10^7$ $M_\odot$) is warm ($\sim$ 100 K), dense (a few $\times 10^5$ cm^{-3}), and rich in OH (X(OH)$\sim 2 \times 10^{-6}$).

- Radiative transfer models that simulate the emission/absorption in all the OH lines have been performed for both the nuclear and the starburst region. The models for the nucleus quantitatively account for the emission in the three OH lines if the nuclear physical conditions pointed out above are assumed. On the other hand, no starburst model is found to match the three OH lines simultaneously, because the strong far-infrared continuum tends to produce absorption, or to weaken the emission, in the OH 119 and 79 μm lines (as observed in other galaxies). Therefore, although some contribution from the extended starburst cannot be ruled out, our models indicate that the bulk of the OH emission arises in the nuclear region. The high nuclear OH abundance required to explain the emission strongly suggest a chemistry deeply influenced by X-rays, i.e., an *X-ray dominated region.*

The authors acknowledge the LWS Consortium, lead by Prof. Peter Clegg, for having built and operated the LWS instrument and solved many instrumental and data reduction problems. We also acknowledge discussions with Dr. Chris Dudley and thank him for reduction and analysis of the ISOCAM 6.2 μm image that we used in this work. The ESA staff at VILSPA (Villafranca, Spain) is also acknowledged for the ISO mission operational support. HAS acknowledges support from NASA Grant NAG5-10659; E.G-A would like to thank the Harvard-Smithsonian Center for Astrophysics for its hospitality while he was in residence during this research. JF acknowledges support from the NASA LTSA program and the Office of Naval Research.

REFERENCES

Alexander, T., Lutz, D., Sturm, E., Genzel, R. et al. 2000, ApJ, 536, 710.

Alloin, D. et al. 2001, A&A, 369, L33.

Ashby, M., et al. 2000, ApJ, 539, L119

Bland-Hawthorn, J., et al., 1997, ApSS, 248, 9.

Blietz, M., Cameron, M., Drapatz, S., Genzel, R. et al. 1994, ApJ, 421, 92.

Bradford, C.M., et al., 1999, Proc.of the Conference "The Universe as seen by ISO", Paris, France, 20-23 October 1998 (ESA SP-427),p.861.

Cameron, M., Storey, J.W.V., Rotaciuc, V., Genzel, R. et al. 1993, ApJ, 419, 136

Clegg, P.E., et al. 1996, A&A, 315, L28.

Colbert, J., et al., 1999, ApJ, 511, 721.

Davies, R.I., Sugai,H., and Ward, M.J., 1998, MNRAS, 300, 388

Draine, B. T. 1985, ApJSS, 57, 587.

Ferland, G.J., 2000, RevMexAA,(Serie de Conferencias), Vol.9, 153

Fischer, J., et al. 1999, Ap&SS, 266, 91.

Goicoechea, J. R., Cernicharo, J. 2002, ApJ, 576, 77.

González-Alfonso, E., & Cernicharo, J. 1997, A&A, 322, 938

González-Alfonso, E., & Cernicharo, J. 1999, ApJ, 525, 845

González-Alfonso, E., Smith, H.A., Fischer, J., Cernicharo, J. 2004, ApJ, 613, 247.

Harvey, V.I., et al., 1999, Proc.of the Conference "The Universe as seeen by ISO", Paris, France, 20-23 October 1998 (ESA SP-427), p.889.

Helfer, T.T., Blitz, L., 1995, ApJ, 450, 90.

Huchra, J.P., Vogeley, M.S. & Geller, M.J. 1999, ApJS, 121, 287.

Kaufman, M.J., Wolfire, M.G., Hollenbach, D.J., Luhman, M.L. 1999, ApJ, 527, 795.

Kessler, M.F. et al.,1996, A&A, 315, L27

Kriss, G.A. et al. 1992, ApJ, 394, L37

Krolik, J.H., & Lepp, S. 1989, ApJ, 347, 179

Ivezic, Z., & Elitzur, M. 1997, MNRAS, 287, 799

Le Floc'h, E., Mirabel, I.F., Laurent, O., Charmandaris, V. et al. 2001, A&A, 367, 487.

Leitherer, C., et al. 1999, ApJS, 125, 489.

Lepp, S., Dalgarno, A. 1996, A&A, 306, 21.

Luhman, M.L. et al. 2003, ApJ, 594, 758.

Lutz, D. et al., 2000,ApJ, 536, 697.

Malhotra, S. et al. 2001, ApJ, 561, 766.

Marconi, A., et al. 1996, A&A, 315, 335.

Malkan, M. A. & Oke, J. B. 1983, ApJ, 265, 92.

Offer, A.R., van Hemert, M.C., & van Dishoeck, E.F. 1994, J. Chem. Phys., 100, 362.

Papadopoulos,P.P. & Seaquist, E.R. 1999, ApJ, 514,L95.

Papadopoulos,P.P. & Seaquist, E.R. 1999, ApJ, 516,114.

Pier, E.A., et al. 1994, ApJ, 428, 124.

Planesas, P., Scoville, N., & Myers, S.T. 1991, ApJ, 369, 364.

Preibisch, T., Ossenkopf, V., Yorke, H.W., Henning, T. 1993, A&A, 279, 577.

Schinnerer, E., et al. 2000, ApJ, 533, 850.

Smith, H.A. 2004, in "Second Workshop on New Concepts for Far Infrared and Submillimeter Space Astronomy", 7-8 March 2002, Univ. Maryland, College Park, Maryland, eds. D. Benford & D. Leisawitz, NASA/CP-2003-212233, p. 98.

Smith, H. A., et al., 2004, in prep.

Spinoglio, L., Andreani, P. & Malkan, M.A., 2002, ApJ, 572, 105.

Spinoglio, L. & Malkan, M.A.,1992, ApJ,399,504.

Scoville, N.Z., Matthews, K., Carico, D.P., Sanders, D.B. 1988, ApJ, 327, L61.

Sternberg, A., Dalgarno, A. 1995, ApJSS, 99, 565.

Sternberg, A., Genzel, R., Tacconi, L. 1994, ApJ, 436, 131.

Swinyard, B.M., et al. 1996, A&A, 315, L43.

Appendix C (paper 2)

Swinyard, B.M., et al. 1998, Proc. SPIE, A.M. Fowler (Ed.), Vol.3354, P.888.

Tacconi, L. J., Genzel, R., Blietz, M., Cameron, M. et al. 1994, ApJ, 426, 77.

Telesco, C.M., et al., 1984, ApJ, 282, 427.

Thatte, N., et al. 1997, ApJ, 490, 238.

Thompson, R.I., 1996, ApJ, 459, L61.

Thronson,H.A. et al. 1989, ApJ, 343, 158.

Usero, A., García-Burillo, S., Fuente, A., Martín-Pintado, J., Rodríguez-Fernández, N.J. 2004, A&A, 419, 897

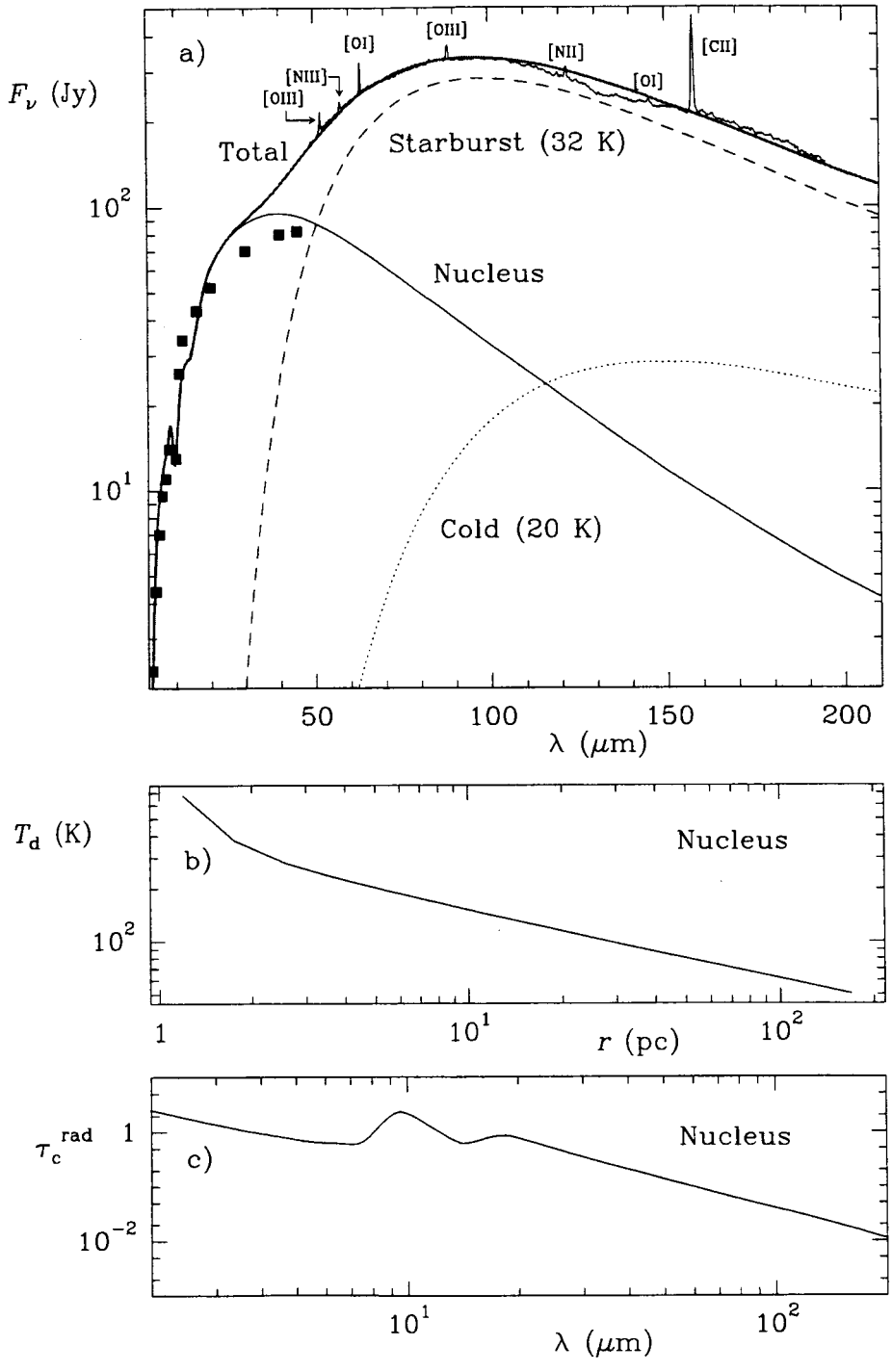

Fig. 1.— a) Spectral energy distribution of NGC 1068 and model fit. Three components, the nucleus, the starburst, and a cold component are used. b) and c) Dust temperature versus the radial position and radial continuum opacity versus wavelength for the nuclear region.

Appendix C (paper 2)

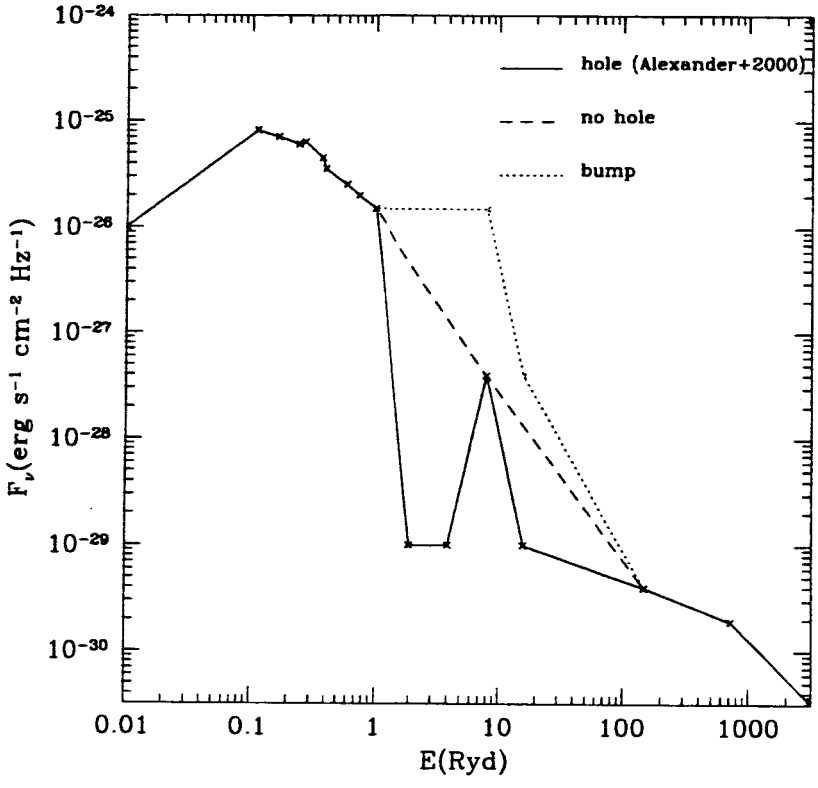

Fig. 2.— The AGN ionizing continua used as input for the photoionization models of NGC 1068. The three continua differ in the frequency region between $1>E_{Ryd}>100$, while outside this region the Pier et al. (1994) spectrum was adopted. The solid line shows the continuum derived from Alexander et al. (2000); the dashed line shows a simple power law interpolation; the dotted line shows the presence of the predicted "big blue bump".

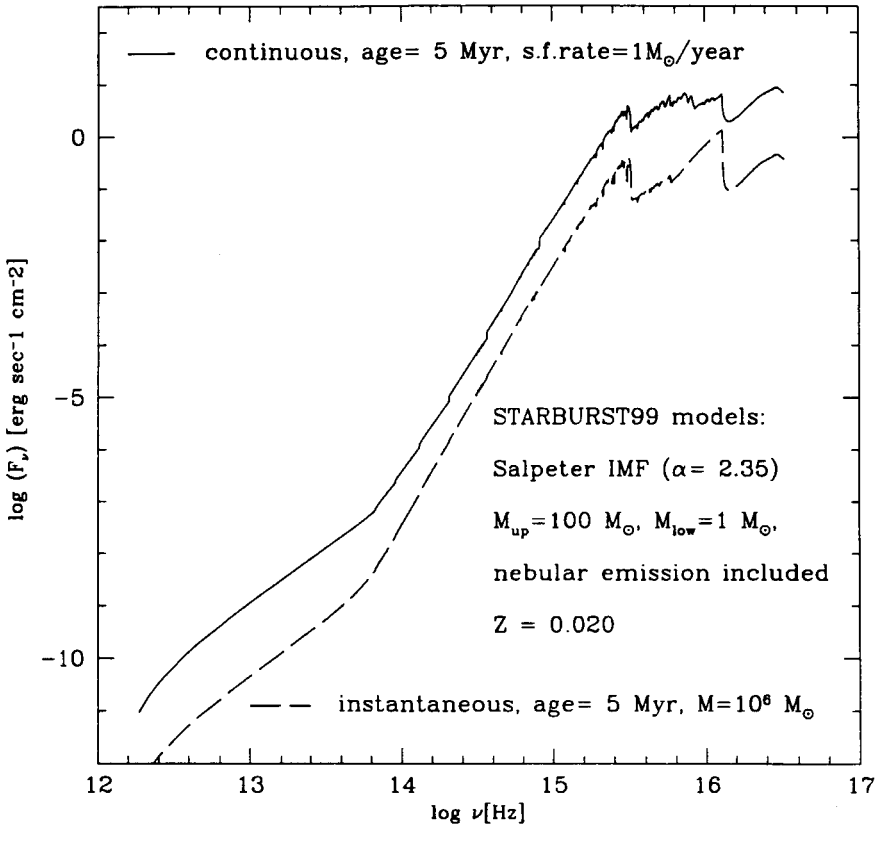

Fig. 3.— The starburst ring ionizing continua used as input for the photoionization models of NGC 1068. The two continua are taken from Leitherer et al. (1999) and represent a continuous starburst model (solid line) and an instantaneous model (broken line), both with 5 Myr of age.

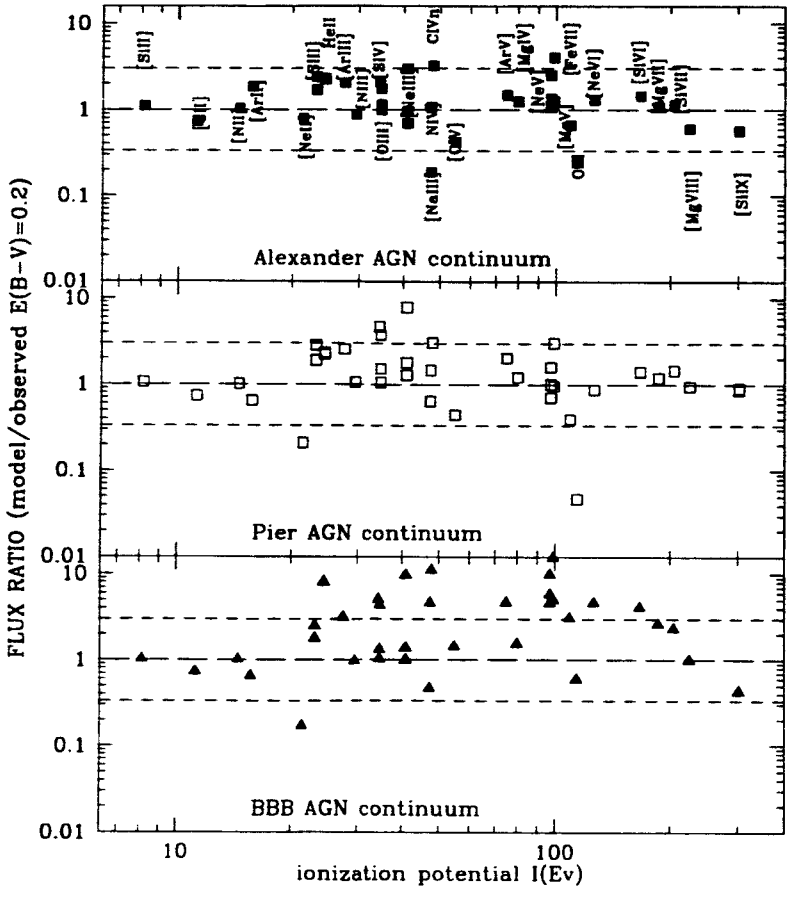

Fig. 4.— The comparison of the composite models with the observations is shown as the ratio of modeled to observed flux ratio for each line, with the ionization potential in the x-axis. The assumed reddening is E(B-V)=0.2. Panels from top to bottom: model CM1, CM2 and CM3. The short dashed lines represent flux ratios within a factor 3 either ways.

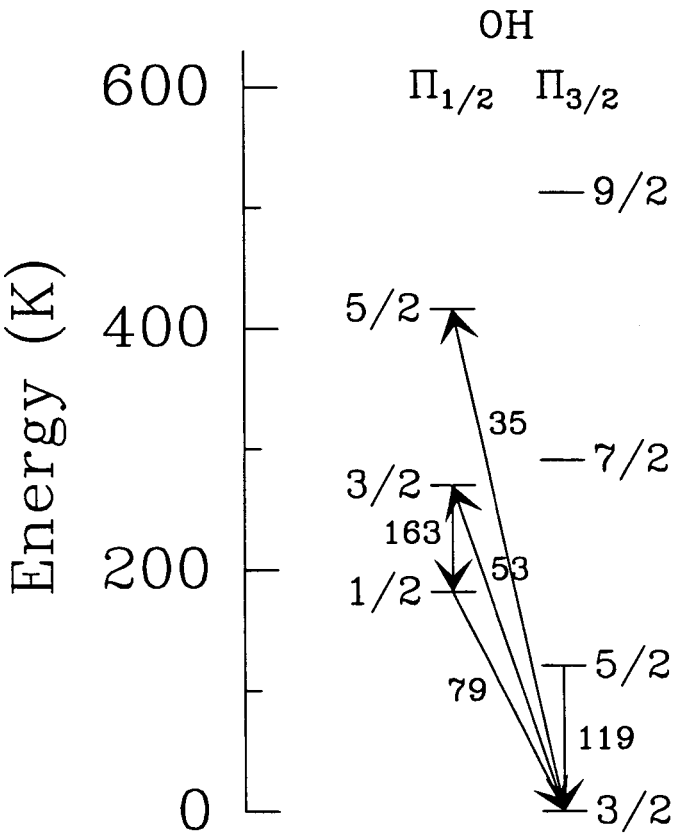

Fig. 5.— Energy level diagram of OH. Rotational levels with energies up to 600 K are shown; the three lines detected in NGC 1068 are indicated with arrows, as well as the 35 and 53 μm lines that could play an important role in the radiative excitation. The wavelengths are indicated in μm. Λ-doubling is ignored because the Λ-doublets are not resolved with the ISO grating resolution.

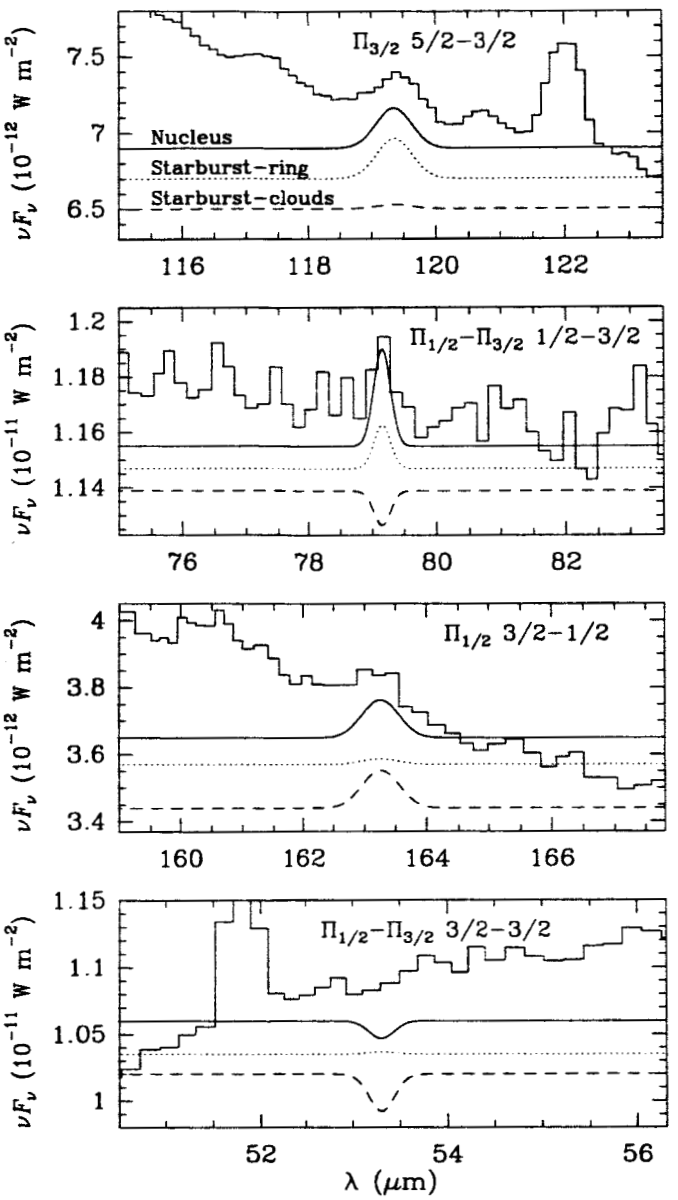

Fig. 6.— Comparison between the observed OH lines and model results. As indicated in the upper panel, the upper modeled spectrum (solid lines) corresponds to the model for the nucleus, the middle one (dotted lines) corresponds to the starburst modelled as a whole, and the lower one (dashed lines) corresponds to the starburst modelled as an ensemble of individual clouds (see text for details).

Table 1. Measured line fluxes from the LWS and SWS grating spectra, with 1σ uncertainties.

Line	λ (μm)	Flux (10^{-13} $erg\ s^{-1}\ cm^{-2}$)	Aperture ($''^2$)	reference
[Si IX] $^3P_2 \rightarrow {}^3P_1$	2.584	3.0	14 × 20	1
[Mg VIII] $^2P_{3/2} \rightarrow {}^2P_{1/2}$	3.028	11. ± 1.1	14 × 20	1
[Si IX] $^3P_1 \rightarrow {}^3P_0$	3.936	5.0 ± 0.6	14 × 20	1
[Mg IV] $^2P_{1/2} \rightarrow {}^2P_{3/2}$	4.487	7.6 ± 1.5	14 × 20	1
[Ar VI] $^2P_{3/2} \rightarrow {}^2P_{1/2}$	4.529	15. ± 3.	14 × 20	1
[Fe II] $^{a4}F_{9/2} \rightarrow {}^{a6}D_{9/2}$	5.340	5.0	14 × 20	1
[Mg VII] $^3P_2 \rightarrow {}^3P_1$	5.503	13.	14 × 20	1
[Mg V] $^3P_1 \rightarrow {}^3P_2$	5.610	18. ± 2.	14 × 20	1
[Ar II] $^2P_{1/2} \rightarrow {}^2P_{3/2}$	6.985	13.	14 × 20	1
[Na III] $^2P_{1/2} \rightarrow {}^2P_{3/2}$	7.318	5.8	14 × 20	1
[Ne VI] $^2P_{3/2} \rightarrow {}^2P_{1/2}$	7.652	110. ± 11.	14 × 20	1
[Fe VII] $^3F_4 \rightarrow {}^3F_3$	7.815	3.0	14 × 20	1
[Ar V] $^3P_2 \rightarrow {}^3P_1$	7.902	< 12.	14 × 20	1
[Na VI] $^3P_2 \rightarrow {}^3P_1$	8.611	< 16.	14 × 20	1
[Ar III] $^3P_1 \rightarrow {}^3P_2$	8.991	23.0 ± 3.3	14 × 20	1
[Fe VII] $^3F_3 \rightarrow {}^3F_2$	9.527	4.0	14 × 20	1
[S IV] $^2P_{3/2} \rightarrow {}^2P_{1/2}$	10.510	58. ± 6.	14 × 20	1
[Ne II] $^2P_{3/2} \rightarrow {}^2P_{1/2}$	12.813	70.	14 × 27	1
[Ar V] $^3P_1 \rightarrow {}^3P_0$	13.102	< 16.	14 × 27	1
[Ne V] $^3P_2 \rightarrow {}^3P_1$	14.322	97. ± 9.7	14 × 27	1
[Ne III] $^3P_1 \rightarrow {}^3P_2$	15.555	160. ± 32.	14 × 27	1
[Fe II] $^{a4}F_{7/2} \rightarrow {}^{a4}F_{9/2}$	17.936	< 10.	14 × 27	1
[S III] $^3P_2 \rightarrow {}^3P_1$	18.713	40.	14 × 27	1
[Ne V] $^3P_1 \rightarrow {}^3P_0$	24.317	70. ± 7.	14 × 27	1
[O IV] $^2P_{3/2} \rightarrow {}^2P_{1/2}$	25.890	190. ± 20.	14 × 27	1
[Fe II] $^{a6}D_{7/2} \rightarrow {}^{a6}D_{9/2}$	25.988	8.	14 × 27	1
[S III] $^3P_1 \rightarrow {}^3P_0$	33.481	55.	20 × 33	1
[Si II] $^2P_{3/2} \rightarrow {}^2P_{1/2}$	34.814	91.	20 × 33	1
[Ne III] $^3P_0 \rightarrow {}^3P_1$	36.013	18.	20 × 33	1
[O III] $^3P_2 \rightarrow {}^3P_1$	51.814	114. ± 3.	80	2
[N III] $^2P_{3/2} \rightarrow {}^2P_{1/2}$	57.317	51.4 ± 2.5	80	2
[O I] $^3P_1 \rightarrow {}^3P_2$	63.184	156. ± 1.	80	2
[O III] $^3P_1 \rightarrow {}^3P_0$	88.356	111. ± 1.	80	2
[N II] $^3P_2 \rightarrow {}^3P_1$	121.897	30.5 ± 1.1	80	2
[O I] $^3P_0 \rightarrow {}^3P_1$	145.525	11.9 ± 0.4	80	2
[C II] $^2P_{3/2} \rightarrow {}^2P_{1/2}$	157.741	216. ± 1.	80	2
OH $^2\Pi_{1/2}5/2$-$^2\Pi_{3/2}3/2$	34.60/34.63	< 3.	20 × 33	2
OH $^2\Pi_{1/2}1/2$-$^2\Pi_{1/2}3/2$	79.11/79.18	14.4 ± 1.5	80	2
OH $^2\Pi_{3/2}5/2$-$^2\Pi_{3/2}3/2$	119.23/119.44	11.9 ± 1.2	80	2
OH $^2\Pi_{1/2}3/2$-$^2\Pi_{1/2}1/2$	163.12/163.40	7.42 ± 0.65	80	2

Note. — (1): from Lutz et al. (2000) and, where errors are available, Alexander et al. (2000); (2): this work

Table 2. Comparison of observed line fluxes with AGN model predictions

Line id.λ (μm)	Observed/D[1] /D[2]	Flux (10^{-13} erg s^{-1} cm^{-2}) AGN A model[3] Comp. 1	AGN A model[3] Comp. 2	AGN B model[4] Comp. 1	AGN B model[4] Comp. 2	AGN C model[5] Comp. 1	AGN C model[5] Comp. 2
O VI λ .1032+.1037	37.4/4334./402.	62.5+33.2	1.5+1.4	12.1+6.4	0.24+0.20	155.+80.	3.2+1.7
$(Ly\alpha)_n$ λ .1215	101.8/3562./602	2806.	1737.	2951.	1828.	3388.	2182.
N IV] λ .1487	5.1/103./22.9	20.0	4.6	28.6	5.0	67.7	38.5
$(CIV)_n$ λ .1549	39.7/790./177.	488.	78.5	462.	83.2	1345.	620.
HeII λ .1640	21.4/426./95.5	96.6	66.5	96.4	67.3	422.	290.
[Ne V] λ .3426	15.7/95./38.7	79.6	17.0	56.2	5.9	288.	94.
[Ne III] λ .3869+.3968	19.2/97./43.2	38.0+11.4	29.8+9.0	145.8+43.9	88.7+26.7	162.+49.	130.+39.
HeII λ .4686	6.1/27.6/13.	13.1	9.6	13.4	9.8	57.8	41.3
[O III] λ .4959+.5007	256./964./496	115.6+334.1	81.3+235	290.+837.	169.+486.	300.+867.	229.+661.
[Si VI] λ 1.96	8.0/9.2/8.6	10.41	2.0	9.7	2.5	30.4	4.8
[Si VII] λ 2.48	8.3	9.38	0.2	11.8	.36	19.0	0.4
[Si IX] λ 2.584	3.0	1.70	···	2.6	···	1.3	—
[Mg VIII] λ 3.028	11.	6.64	···	10.5	···	11.	—
[Si IX] λ 3.936	5.4	3.10	···	4.9	···	2.3	—
[Mg IV] λ 4.487	7.6	3.21	6.2	3.5	5.8	11.2	0.5
[Ar VI] λ 4.529	15.	14.9	7.3	24.1	6.6	39.2	31.
[Mg VII] λ 5.503	13.	13.9	0.23	15.6	.14	33.2	0.8
[Mg V] λ 5.610	18.	5.62	6.31	4.0	3.1	31.6	23.9
[Ar II] λ 6.985	13.	6.87	13.4	1.3	3.1	1.4	3.1
[Na III] λ 7.318	5.8	0.66	0.45	2.2	1.4	1.5	1.1
[Ne VI] λ 7.652	110.	134.	8.8	93.7	2.6	455.	54.
[Fe VII] λ 7.815	3.0	1.92	1.90	1.9	1.0	8.6	6.4
[Ar V] λ 7.902	< 12.	2.90	1.91	3.3	2.5	4.5	7.0
[Na VI] λ 8.611	< 16.	1.10	0.18	0.8	.08	3.8	0.8
[Ar III] + [Mg VII] λ 8.991	25.	17.8+17.	9.0+0.36	18.2+19.4	19.+.19	16.+40.	15.3+1.0
[Fe VII] λ 9.527	4.0	7.96	8.2	7.7	4.5	35.3	26.8
[S IV] λ 10.510	58.	76.5	43.6	155.	117.	133.	161.
[Ne II] λ 12.813	70.	24.8	23.9	2.9	6.0	1.9	4.3
[Ar V] λ 13.102	< 16.	2.94	2.86	3.4	3.7	4.7	10.3
[Ne V] λ 14.322	97.	79.2	50.7	74.6	23.7	332.	232.
[Ne III] λ 15.555	160.	68.1	37.6	136.7	104.	91.4	79.6
[S III] λ 18.713	40.	33.7	41.5	31.5	61.9	28.2	51.3
[Ne V] λ 24.317	70.	34.8	39.8	31.2	18.2	139.	182.
[O IV] λ 25.890	190.	22.2	55.4	25.6	57.5	69.6	200.
[S III] λ 33.481	55.	8.59	26.3	7.7	38.1	6.7	33.1
[Si II] λ 34.814	91.	11.2	39.5	8.6	38.5	5.9	37.1
[Ne III] λ 36.013	18.	4.97	3.2	10.2	8.8	6.9	6.8
[O III] λ 51.814	110.	19.2	27.3	28.2	59.5	19.8	44.7
[N III] λ 57.317	51.	4.64	8.7	4.9	17.4	3.7	14.4
[O I] λ 63.184	156.	2.50	3.6	1.5	3.7	0.9	3.8
[O III] λ 88.356	110.	2.53	6.5	3.8	14.2	2.6	11.3
[N II] λ 121.897	30.	0.13	0.86	.06	.40	.08	0.5
[O I] λ 145.525	12.	0.16	0.28	.09	.29	.05	0.3
[C II] λ 157.741	220.	0.46	3.1	.29	2.2	.11	1.8

Table 2—Continued

Line id.λ (μm)	Observed/D[1] /D[2]	Flux (10^{-13} erg s^{-1} cm^{-2}) AGN A model[3] Comp. 1	AGN A model[3] Comp. 2	AGN B model[4] Comp. 1	AGN B model[4] Comp. 2	AGN C model[5] Comp. 1	AGN C model[5] Comp. 2

[1]Dereddened line flux, assuming $E_{B-V} = 0.4$

[2]Dereddened line flux, assuming $E_{B-V} = 0.2$

[3]AGN A parameters: component 1: Log U=-1., Log n=4, internal radius $\simeq$ 21 pc, external radius $\simeq$ 109 pc, ionizing spectrum from Alexander et al. (2000): component 2: Log U=-2., Log n=3.3, internal radius $\simeq$ 153 pc, external radius $\simeq$ 362 pc, ionizing spectrum from Alexander et al. (2000).

[4]AGN B parameters: same as AGN A models, but with the ionizing spectrum from Pier et al. (1994)

[5]AGN C parameters: same as AGN A models, but with the ionizing spectrum that includes a big blue bump (see text)

Table 3. Comparison of observed line fluxes with the Ring Starburst model predictions

Line id.λ (μm)	Observed	Flux (10^{-13} erg s^{-1} cm^{-2}) SBR A[1]	SBR B[2]	SBR C[3]	SBRD[4]	SBR E[5]	SBR F[6]
O VI λ .1032+.1037	37.4/4334./402.	—	—	—	—	—	—
$(Ly\alpha)_n$ λ .1215	101.8/3562./602	221.	36.3	284.	400.	1135.	1424.
N IV] λ .1487	5.1/103./22.9	22.8	0.02	41.8	0.02	177.	0.08
$(CIV)_n$ λ .1549	39.7/790./177.	162.	0.39	277.	.75	1154.	1.80
HeII λ .1640	21.4/426./95.5	235.	38.9	373.	47.8	1466.	161.
[Ne V] λ .3426	15.7/95./38.7	16.2	—	30.9	—	125.	—
[Ne III] λ .3869+.3968	19.2/97./43.2	106.+32.	24.6+7.4	165+49.7	30.4+9.2	659+199	105+31.6
HeII λ .4686	6.1/27.6/13.	33.5	5.8	53.1	7.1	207.	23.8
[O III] λ .4959+.5007	256./964./496	439+1269	19.8+57.	720+2077	24.6+71.2	2882+8307	85.8+247.
[Si VI] λ 1.96	8.0/9.2/8.6	—	—	—	—	—	—
[Si VII] λ 2.48	8.3	—	—	—	—	—	—
[Si IX] λ 2.584	3.0	—	—	—	—	—	—
[Mg VIII] λ 3.028	11.	—	—	—	—	—	—
[Si IX] λ 3.936	5.4	—	—	—	—	—	—
[Mg IV] λ 4.487	7.6	1.0	—	1.7	—	6.6	—
[Ar VI] λ 4.529	15.	1.7	—	3.3	—	13.3	—
[Mg VII] λ 5.503	13.	—	—	—	—	—	—
[Mg V] λ 5.610	18.	0.84	—	1.6	—	6.2	—
[Ar II] λ 6.985	13.	2.6	3.3	3.1	4.0	11.7	13.6
[Na III] λ 7.318	5.8	0.2	0.09	0.3	0.1	1.2	0.4
[Ne VI] λ 7.652	110.	4.5	—	8.0	—	35.	—
[Fe VII] λ 7.815	3.0	0.13	—	0.3	—	1.2	—
[Ar V] λ 7.902	< 12.	1.9	—	4.0	—	15.6	—
[Na VI] λ 8.611	< 16.	—	—	—	—	—	—
[Ar III] + [Mg VII] λ 8.991	25.	16.	5.6	23.	6.9	89.7	23.1
[Fe VII] λ 9.527	4.0	0.6	—	1.1	—	4.3	—
[S IV] λ 10.510	58.	91.	0.6	157.	0.8	589.	2.4
[Ne II] λ 12.813	70.	3.3	4.9	3.9	5.8	15.2	20.4
[Ar V] λ 13.102	< 16.	5.7	—	10.6	—	41.4	—
[Ne V] λ 14.322	97.	74.4	—	134.	—	524.	—
[Ne III] λ 15.555	160.	97.3	40.3	143.	48.7	552.	163.
[S III] λ 18.713	40.	65.3	1.6	99.	20.3	386.	69.
[Ne V] λ 24.317	70.	83.6	—	148.	—	490.	—
[O IV] λ 25.890	190.	496.	1.4	828.	1.7	2615	4.7
[S III] λ 33.481	55.	199.	51.	279.	58.4	649.	125.
[Si II] λ 34.814	91.	45.8	45.	53.	49.3	105.	100.
[Ne III] λ 36.013	18.	17.4	6.9	26.	4.3	97.	28.
[O III] λ 51.814	110.	921.	62.	1559.	80.4	4800.	222.
[N III] λ 57.317	51.	349.	30.	468.	31.8	750.	44.4
[O I] λ 63.184	156.	65.	99.	77.	120.	300.	383.
[O III] λ 88.356	110.	1539.	105.	1812.	99.5	1830.	90.
[N II] λ 121.897	30.	30.*	30*	30.*	30.*	30.*	30.*
[O I] λ 145.525	12.	6.5	10.	7.7	12.	27.	36.
[C II] λ 157.741	220.	294.	377.	130.	158.	1440.	145.

Note. — *: this line was used for normalization

[1]SBR A parameters: Log U=-2.5, Log n=1.0, ionizing spectrum from Starburst99 with instantaneous star-formation law, M = $10^6 M_\odot$, IMF: =2.35 $M_{up} = 100 M_\odot$, $M_{low} = 1 M_\odot$, nebular emission included, Z=0.020, age of 5 Myr. The integration was stopped at a temperature of 50K, the adopted abundances are those relative to HII regions and grain emission is included.

[2]SBR B parameters: Log U=-3.5, Log n=1.0, all other parameters as for SBR A.

[3]SBR C parameters: Log U=-2.5, Log n=2.0, all other parameters as for SBR A.

[4]SBR D parameters: Log U=-3.5, Log n=2.0, all other parameters as for SBR A.

[5]SBR E parameters: Log U=-2.5, Log n=3.0, all other parameters as for SBR A.

[6]SBR F parameters: Log U=-3.5, Log n=3.0, all other parameters as for SBR A.

Table 4. Comparison of observed line fluxes with composite model predictions

Line id.λ (μm)	Flux (10^{-13} erg s^{-1} cm^{-2}) Observed/D[1] /D[2]	CM1[3]	CM2[4]	CM3[5]
O VI λ .1032+.1037	37.4/4334./402.	98.6	18.9	240.
$(Ly\alpha)_n$ λ .1215	101.8/3562./602	4943.	5179	5970.
N IV] λ .1487	5.1/103./22.9	24.6	33.8	106.2
$(CIV)_n$ λ .1549	39.7/790./177.	567.	546	1967.
HeII λ .1640	21.4/426./95.5	211.	211.5	761.
[Ne V] λ .3426	15.7/95./38.7	96.6	62.1	382.
[Ne III] λ .3869+.3968	19.2/97./43.2	127.8	344.7	420.
HeII λ .4686	6.1/27.6/13.	29.8	30.3	106.2
[O III] λ .4959+.5007	256./964./496	861.8	1879	2153.
[Si VI] λ 1.96	8.0/9.2/8.6	12.4	12.2	35.2
[Si VII] λ 2.48	8.3	9.6	12.2	19.4
[Si IX] λ 2.584	3.0	1.7	2.6	1.3
[Mg VIII] λ 3.028	11.	6.6	10.5	11.
[Si IX] λ 3.936	5.4	3.1	4.9	2.3
[Mg IV] λ 4.487	7.6	9.4	9.3	11.7
[Ar VI] λ 4.529	15.	22.	30.7	70.2
[Mg VII] λ 5.503	13.	14.	15.7	34.
[Mg V] λ 5.610	18.	12.	7.1	55.5
[Ar II] λ 6.985	13.	24.	8.4	8.5
[Na III] λ 7.318	5.8	1.1	3.7	2.7
[Ne VI] λ 7.652	110.	143	96.3	509.
[Fe VII] λ 7.815	3.0	3.8	2.9	15.
[Ar V] λ 7.902	$<$ 12.	4.8	5.8	11.5
[Na VI] λ 8.611	$<$ 16.	1.3	0.9	4.6
[Ar III] + [Mg VII] λ 8.991	25.	51.	64.1	79.2
[Fe VII] λ 9.527	4.0	16.	12.2	62.1
[S IV] λ 10.510	58.	121	273.	295.
[Ne II] λ 12.813	70.	55.	14.7	12.
[Ar V] λ 13.102	$<$ 16.	5.8	7.1	15.
[Ne V] λ 14.322	97.	130.	98.3	564.
[Ne III] λ 15.555	160.	155.	289.4	220.
[S III] λ 18.713	40.	95.	113.7	99.8
[Ne V] λ 24.317	70.	75.	49.4	321.
[O IV] λ 25.890	190.	80.	84.8	272.
[S III] λ 33.481	55.	93.	104.2	98.2
[Si II] λ 34.814	91.	100.	96.4	92.3
[Ne III] λ 36.013	18.	12.5	23.3	18.
[O III] λ 51.814	110.	127	168.1	145.
[N III] λ 57.317	51.	45.	54.1	50.
[O I] λ 63.184	156.	126.	125.2	125.
[O III] λ 88.356	110.	109.	117.5	113.
[N II] λ 121.897	30.	31.	30.5	30.6
[O I] λ 145.525	12.	12.4	12.4	12.3
[C II] λ 157.741	220.	161	160.4	160.

[1]Dereddened line flux, assuming $E_{B-V} = 0.4$

[2]Dereddened line flux, assuming $E_{B-V} = 0.2$

^{3}CM1 = AGN A + SBR D

^{4}CM2 = AGN B + SBR D

^{5}CM3 = AGN C + SBR D

Appendix C (paper 2)

Table 5. Comparison of observed line fluxes with model predictions for the nuclear region

Line id.λ	Flux (10^{-12} $erg\ s^{-1}\ cm^{-2}$) Observed	Modeled	Notes
34μm	< 0.1	-0.70	(absorption)
53μm	< 1.2	-0.84	(absorption)
79μm	1.44	1.46	
84μm	< 1.2	0.16	
98μm	< 1.2	0.31	
119μm	1.19	1.52	
163μm	0.74	0.51	